Acta Crystallographica Section B
Structural Science
ISSN 0108-7681

Structure of oxidized bismuth nanoclusters

K. J. Stevens,[a,b]* B. Ingham,[c,d] M. F. Toney,[c] S. A. Brown,[b,e] J. Partridge,[b,e] A. Ayesh[b,e] and F. Natali[e]

[a]MPT Solutions Ltd, PO Box 38-096, Lower Hutt, New Zealand, [b]The MacDiarmid Institute for Advanced Materials and Nanotechnology, PO Box 600, Wellington, New Zealand, [c]Stanford Synchrotron Radiation Laboratory, 2575 Sand Hill Rd, MS69, Menlo Park, CA 94025, USA, [d]Industrial Research Ltd, PO Box 31-310, Lower Hutt, New Zealand, and [e]Nanostructure Engineering Science and Technology Group, Department of Physics and Astronomy, University of Canterbury, Private Bag 4800, Christchurch, New Zealand

Correspondence e-mail: k.stevens@mptsolutions.com

Received 22 March 2007
Accepted 19 May 2007

Synchrotron X-ray diffraction has determined that β-Bi_2O_3 is the dominant oxide phase covering hexagonal bismuth nanoclusters produced in an inert gas aggregation source. Simulated Debye–Scherrer patterns have indicated that the oxide is 20 ± 5 Å thick on average, at the surface of 320 ± 40 Å diameter clusters. A Williamson–Hall analysis of the peak broadening was used to measure the non-uniform strain in clusters. The oxidized clusters were in $-0.11 \pm 0.06\%$ uniform compressive strain compared with other clusters without oxides detectable by X-ray diffraction which only have a small tensile uniform strain. High-resolution transmission electron microscopy (HRTEM) and multislice image simulations indicated a β-Bi_2O_3 thickness of 20–50 Å. The HRTEM micrographs show the relative orientation between the oxide and the cluster core.

1. Introduction

Bismuth nanowires can be fabricated by the coalescence of clusters into V grooves in silicon wafers fabricated using conventional electron-beam lithography. The resulting wires have a complex structure. Bismuth is a semi-metal in the bulk form, but there is a transition from semi-metal to semiconductor at a wire diameter of ~ 500 Å owing to quantum confinement effects (Lin *et al.*, 2000), and thus these wires are an interesting system for the study of fundamental physics at the nanoscale. Bismuth also has many desirable electrical properties such as a long mean-free path (1000 Å at 300 K) and a low charge-carrier density. Nanocluster devices intrinsically possess large surface area to volume ratios and will form surface oxide films. It is often the properties of the surface films of thin oxides that control the technologically important functionality of such metallic nanoparticles. For example, the composition and structure of a surface oxide layer will be critical for applications using bismuth nanowires and may influence the electromigration properties of such wires.

The electron diffraction of a beam of unsupported bismuth clusters in a vacuum is a method for the direct study of the unoxidized cluster structure (Wurl, 2003). Crucially, the clusters are free from interaction with a substrate, or from surface contamination, which might otherwise alter the delicate balance of energies determining the structure. In earlier work, nanometre-scale atomic clusters were produced in an inert-gas aggregation source collimated into a molecular beam that was then probed by high-energy electrons (100 keV) under high-vacuum conditions, milliseconds after their creation, to obtain electron-diffraction patterns (Hall *et al.*, 1991). Determining cluster structure using electron or X-ray diffraction (XRD) patterns from clusters requires consideration of an ensemble

Table 1
Sample preparation conditions including Ar and He flow rates.

1 sccm = 1 standard centimeter cube per minute = 1 cm^3 per minute at 273 K and deposition system pressure. The high-vacuum (HV) system produces a non-uniform spot so the monolayer thickness has not been tabulated. The nominal thickness listed is the equivalent thickness if all the cluster atoms were spread evenly over the substrate surface. The clusters are not coalesced uniformly and have a larger diameter than the nominal thickness because the typical cluster coverage on the surface is 60–70%.

Sample	Ar (sccm)	He (sccm)	Deposition system	Thickness (Å)
Bi oxide XRD and TEM	60–100	0	HV	–
BI01	100	25	UHV	180
BI03	100	100	UHV	180
BIAO17, 19, 24	100	0	UHV	200

of clusters with a distribution of sizes, structures (icosahedral, decahedral, amorphous or bulk) and orientations. It is not possible to rapidly oxidize an unsupported beam of clusters and then probe it with electrons whilst still unsupported owing, in part, to the low-scattering path distance of electrons in air and to the oxidation rates of most metals. XRD is a more relevant technique for determining the oxide structure and its effects upon the cluster structure and strain, but at present the technique does necessitate the use of supported clusters. High-intensity synchrotron radiation is required because the small clusters and thin oxide films on the surfaces do not give a sufficient signal with conventional XRD sources. In the first instance, the diffraction data is analyzed using simulated Debye–Scherrer patterns produced using the bulk bismuth rhombohedral or hexagonal structure and bismuth oxide phases.

Previous synchrotron work on intentionally oxidized bismuth involved polycrystalline evaporated bismuth films that were deposited in a vacuum and then exposed to 10^{-8}–10^{-3} Torr pressure oxygen for 100–10 000 s at room temperature (Benbow & Hurych, 1976) and has concentrated on the band structure of a bismuth oxide phase (probably α-Bi_2O_3). Other significant synchrotron spectroscopy has been undertaken on oxidized bismuth silicate glasses which identified the α-Bi_2O_3 phase (Witkowska *et al.*, 2005). X-ray absorption spectroscopy (as both EXAFS or XANES) have been used to probe the oxide structure, the nearest-neighbour spacings and the stoichiometry of the bond to the metal atoms of the cluster (Stevens *et al.*, 2005). Attempts can be made to control the oxide structure and properties by varying the environmental conditions during oxide formation. Experimentally, bismuth cluster-assembled nanowires have been oxidized in wet and/or oxygenated, low-temperature environments, while the performance of the wires was monitored by resistance measurement, which is capable of detecting monolayer oxidation (Cai & Lyon, 2003).

In this work HRTEM has been used to estimate oxide thickness, cluster diameter and structure as the initial parameters for the fitting of the synchrotron X-ray diffraction spectra. HRTEM can show the projected two-dimensional structure of certain clusters, but is reliant on obtaining a favourable orientation and has a poorer ability to characterize a larger ensemble. A JEOL2010HR TEM has been used for direct imaging of supported cluster structure and faceting. The interpretation of HRTEM micrographs is based on calculated images of candidate structures, obtained using multislice electron-wave scattering software (Flüeli, 1989). A review of HRTEM of bismuth clusters is given in Stevens *et al.* (2005).

2. Sample preparation and experimental method

In this work 300–500 Å diameter bismuth clusters were deposited onto amorphous carbon films supported on copper TEM grids by a gas aggregation method in a mixture of argon and helium gas flow. The samples became oxidized in air during transfer from the deposition system to a Jeol 2010 HRTEM. As the sample preparation is carried out in different locations from the TEM and XRD, there can be several months between preparation and examination of the samples (depending on the availability of equipment), during which time oxidation in air occurs. The same conditions as used for HRTEM sample preparation were used for the deposition of clusters onto a smooth silicon wafer (native oxide only) for synchrotron XRD measurements. The sample preparation conditions are shown in Table 1; by varying the Ar and He inert-gas ratio and flow rates some control is afforded over the particle diameter. Grazing incidence XRD (GIXRD) work was undertaken on beamline 7–2 (http://www-ssrl.slac.stanford.edu/beamlines/bl7-2), and the specular X-ray diffraction on beamline 2–1 (http://www-ssrl.slac.stanford.edu/beamlines/bl2-1), at the Stanford Synchrotron Radiation Laboratory (SSRL) using a focused X-ray beam with wavelengths of 1.549 (for samples BIAO17, 19 and 24 in Table 1), 1.409 (for the Bi oxide sample) and 1.545 Å (for samples BIO1 and BIO3), respectively. Soller slits of 1 milliradian were used on the diffracted beam analyzer and the diffracted X-rays were detected with a liquid-nitrogen-cooled Ge detector. The incident X-ray angle was set just above the critical angle for the total reflection of the X-rays from the Bi nanoclusters. In the GIXRD geometry the scattering vector is nearly in the plane of the substrate; for specular XRD the scattering plane lies normal to the substrate. Our data were obtained as a function of scattering vector $|\mathbf{Q}| = 2\pi S = 2\pi|\mathbf{g}|$, typically running from $\mathbf{Q}$ = 1.0 to 6.0 $Å^{-1}$.

3. Bismuth oxide crystallography

Bulk bismuth has the space group $R\bar{3}m$ (No. 166); in this paper the hexagonal axes of the trigonal structure have been employed (instead of the alternative rhombohedral axes), with $a = b = 4.546$ (2) and $c = 11.862$ (6) Å (Cucka & Barrett, 1962). Bi_2O_3 has four common phases (Harwig, 1978). Most current research focuses on the higher-temperature phase, δ-Bi_2O_3, which has high oxide-ion conductivity with applications in solid-oxide fuel cells (Sammes *et al.*, 1999). α-Bi_2O_3 occurs below 100 K, has a monoclinic structure, space group $P2_1/c$

(No. 14) with a = 5.8496 (3), b = 8.1648 (4), c = 7.5101 (4) Å and β = 112.977 (3)° (Cai & Lyon, 2003; Harwig, 1978), and was therefore initially thought to be the most likely to occur on the surface of the bismuth nanoclusters in the present work. Another candidate oxide phase is β-Bi_2O_3, which has a tetragonal structure [space-group number $P\bar{4}2_1c$ (No. 114) with a = 7.739 (1), c = 5.636 (1) Å (Blower & Greaves, 1988)] and is usually only metastable at room temperature. Other candidate oxides are γ-Bi_2O_3, which is a body-centred cubic phase, space group $I23$ (No. 197), with a = 10.268 (1) Å, and δ-Bi_2O_3, which is a face-centred cubic phase, space group $Fm\bar{3}m$ (No. 225), with a = 5.66 (2) Å (powder diffraction file; http://www.icdd.com; Harwig & Gerards, 1979).

4. Results

A kinematic calculation of the XRD intensities from the four candidate oxides and bulk bismuth is shown in Fig. 1, along with an experimental GIXRD pattern from a bismuth cluster sample that exhibited diffraction from a Bi oxide. β-Bi_2O_3 is the best fit to the peaks that are not matched by the bulk bismuth. It is unusual for β-Bi_2O_3 to be the dominant bismuth oxide phase at room temperature, as described in the phase diagrams in the review paper of Shuk *et al.* (1996) and an earlier paper by Harwig & Gerards (1979). We have only observed clear β-oxide phase peaks in one of the 16 bismuth samples examined (which we refer to as the oxidized Bi cluster sample). In the other 15 samples the largest (012) bismuth peak around S = 0.305 Å^{-1} is much broader than expected from the size of the clusters. The broadening is thought to be associated with a thinner layer of bismuth oxide of a phase that we cannot conclusively identify with XRD, or increased levels of disorder owing to stacking faults or movement of the bismuth atoms near the oxide.

The Debye–Scherrer pattern from a cluster ensemble when two atom types are present is given by

$$I(S) = c(S)\sum_{j=1}^{N_A}\sum_{k=1}^{N_B} f^A(S)f^B(S)e^{2\pi i g.r_{jk}} = c(S)\sum_{j=1}^{N_A}\sum_{k=1}^{N_B} f^A(S)f^B(S)\frac{\sin(2\pi S r_{jk})}{2\pi S r_{jk}}, \quad (1)$$

where $f^A(S)$ is the X-ray scattering factor for the A-type atoms, r_{jk} is the distance between the jth atom A and kth atom B, and $c(S)$ is a prefactor that includes the Lorentz polarization and Debye–Waller factors. The second term arises from the first, by a spherical average of the intensity from the model cluster over all diffracting vectors **g**, to give a pattern that is a function of the magnitude of **g** = S (Hall *et al.*, 1995; Birkholz, 2006). Equation (1) differs from the conventional $(\sin(x)/x)^2$-type function for a diffraction pattern that arises from squaring a Fourier transform over a rectangular region of space with long-range order, because when we have an ensemble of clusters, each cluster of crystalline material has no preferred orientation with respect to the other clusters. Equation (1) is derived after a further integration has been made to find the orientational average. The X-ray scattering factors of Rez *et al.* (1994) have been used in the simulations. The simulation code was developed to place an oxide film on a facetted bismuth core to determine the average oxide thickness more accurately. Fig. 2 shows the same GIXRD pattern as in Fig. 1, from a sample of bismuth clusters with several layers of surface oxide (sufficient to form oxide peaks) created by exposure to ambient air, and simulated Debye–Scherrer patterns from the β-Bi_2O_3 and bulk bismuth. The peak positions and phases were matched to the bulk bismuth structure and β-Bi_2O_3. The Debye–Scherrer simulations of the experimental data indicate an ensemble average sphere diameter of 320 ± 40 Å of bismuth

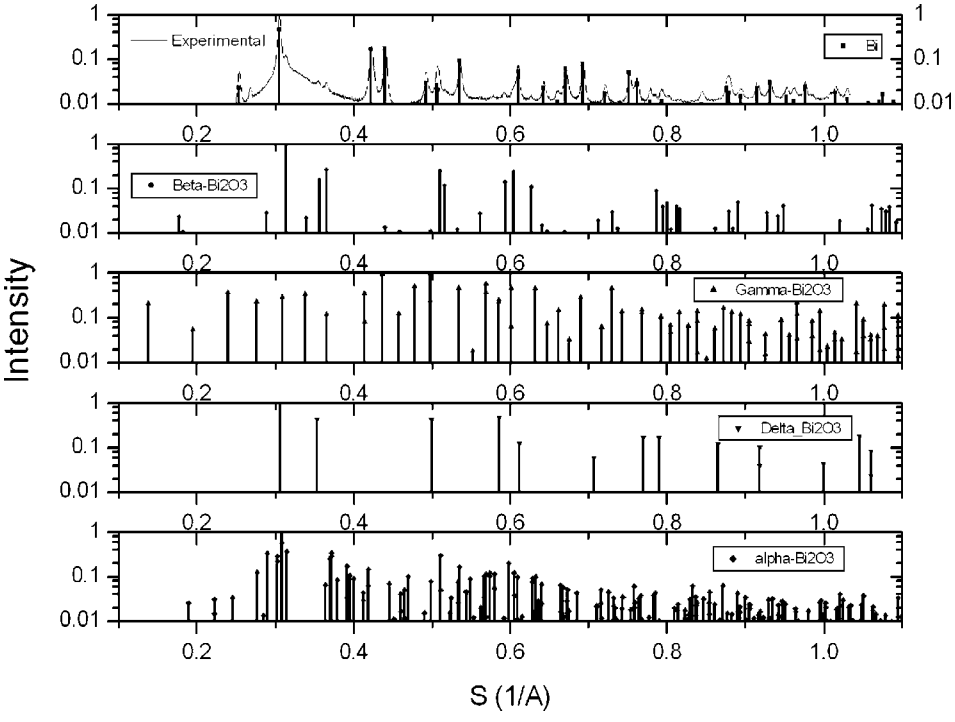

Figure 1
The top panel shows an experimental synchrotron GIXRD pattern, corrected for Lorentz polarization, from oxidized bismuth clusters and the peak positions and relative intensities expected from a kinematic calculation of X-ray diffraction from bulk bismuth. The other panels show the peak position and heights for the four alternative bismuth oxide structures. β-Bi_2O_3 is the best fit to the peaks (mainly the three peaks between 0.314 and 0.365 Å^{-1}) that are not matched by the bulk bismuth. The experimental peak at 0.268 Å^{-1} matches the position of a bismuth peak, but it is larger than predicted by kinematic calculations for bismuth, because of significant texture in the sample.

surrounded by a 20 ± 5 Å thick shell of β-Bi_2O_3. The core diameter and oxide thickness in the model have been chosen to match the experimental peak widths. Increasing the diameter of the bismuth core gives sharper peaks that are of higher relative intensity compared with the oxide shell. The total core and shell particle diameters agree with FEG SEM images of the sample.

Larger clusters can be formed from several crystalline domains due to the presence of lattice defects (*e.g.* dislocations and stacking faults), and calculated Debye–Scherrer simulations are dominated by the structure of the domains (Wurl, 2003), so Debye–Scherrer fits indicate the mean crystalline domain size and can underestimate the cluster diameter. Note in Fig. 2 that the relative intensities of the simulated and experimental patterns do not match up exactly, which probably indicates the influence of texturing, surface reconstruction due to the oxide, and internal disorder such as stacking faults which have broadened the strongest bismuth peak near $S = 0.305$ Å^{-1}. The presence of texture was confirmed using SSRL beamline 11–3 and using specular scans on SSRL beamline 7–2.

The observation of β-Bi_2O_3 is a significant result which will probably affect the electromigration behaviour, as β-Bi_2O_3 is a fast-ion conductor, whereas α-Bi_2O_3 is a hole-carrier conductor (Harwig & Gerards, 1978). The β-Bi_2O_3 phase also has a significantly higher electrical conductivity. Electrical changes in nanowire resistance follow a power law during overnight exposures to oxygen immediately after cluster

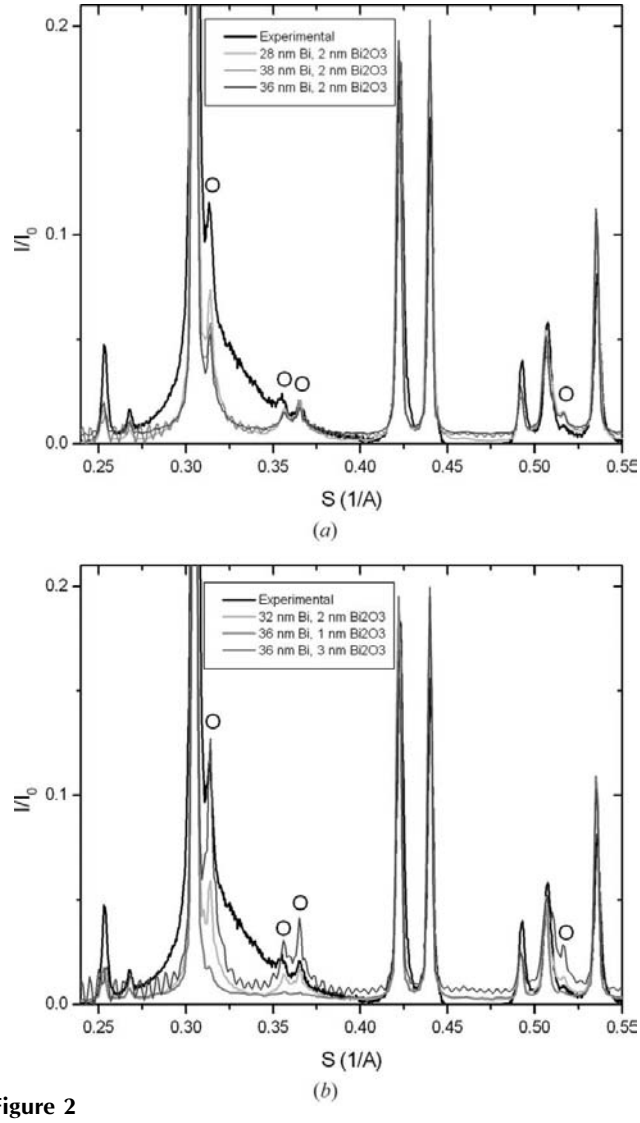

Figure 2
Experimental synchrotron GIXRD pattern ($S = 1/d$, where d is the lattice plane spacing) from oxidized bismuth clusters. The experimental curve has been compared in (*a*) and (*b*) to simulated Debye–Scherrer patterns calculated from a 280–380 Å diameter solid sphere of bismuth and surrounded by a 10–30 Å thick shell of β-Bi_2O_3. The experimental intensity corrected for Lorentz polarization has been normalized to 1.0 at the largest peak and the simulated intensity with room-temperature Debye–Waller factors has been scaled to agree with the two bismuth peaks near $S = 0.42$ and 0.44 Å^{-1}. The oxide peaks are indicated by the 'O' text.

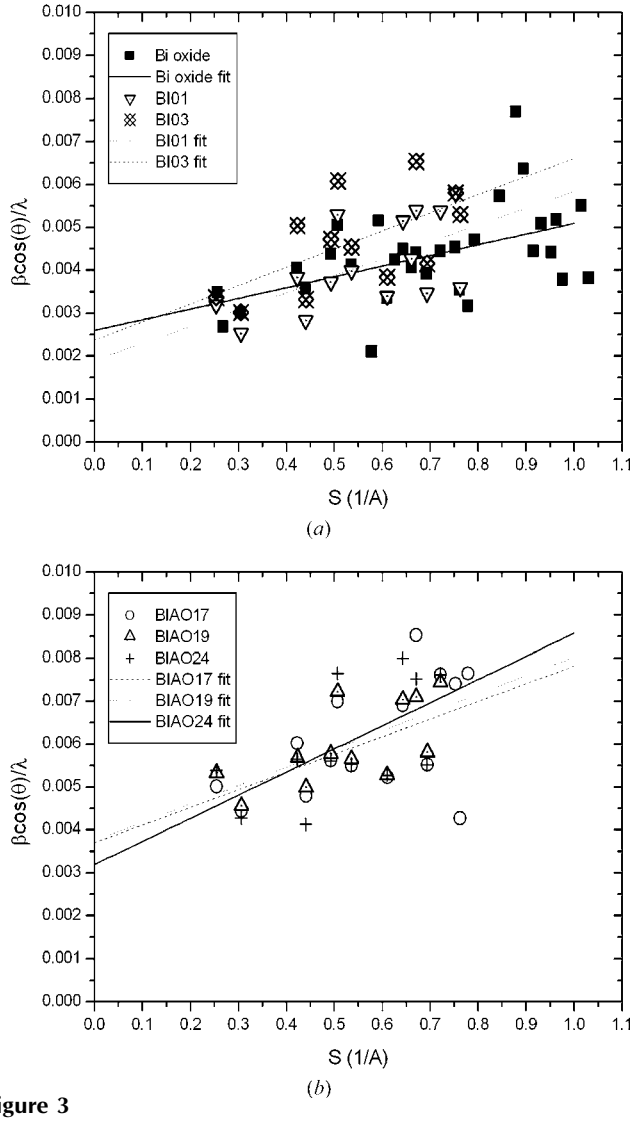

Figure 3
Williamson–Hall analysis of the average non-uniform strain (from the slope of the linear fit) and diameter (from the intercept) of the bismuth nanoclusters determined from peak broadening. (*a*) Analysis of samples Bi oxide, BI01 and BI03. (*b*) Analysis of samples BIAO17, BIAO19 and BIA024.

Table 2
Williamson–Hall analysis of particle diameter and average magnitude of non-uniform strain from the peak broadening.

The uniform strain is calculated from the peak shift.

Sample	Bismuth core diameter t (Å)	Peak-broadening non-uniform strain (%)	Peak-shift uniform strain (%)
Bi oxide	350 (80)	0.25 (8)	−0.11 (6)
BI01	500 (200)	0.4 (1)	0.07 (5)
BI03	400 (200)	0.4 (2)	0.16 (8)
BIAO17	240 (70)	0.4 (2)	0.07 (5)
BIAO19	240 (50)	0.4 (2)	0.06 (5)
BIAO24	300 (100)	0.5 (2)	0.05 (7)
BIAO17, 19 and 24 average	260 (50)	0.5 (1)	0.06 (3)

nanowire fabrication (Parquez *et al.*, 2007). Note that the largest bismuth experimental peaks are at larger S than the simulated peak positions, which is due to 0.11% compressive uniform strain in the nanoparticles. The largest experimental bismuth oxide peak at 0.313 Å^{-1} has peaks at lower S than the simulated peaks, indicating a tensile strain of about 0.3% in the oxide. The strain in the clusters will be altered from an unoxidized cluster by the epitaxic mismatch in lattice constants of the oxide on the bismuth core. Anisotropic materials will have lattice planes with different elastic constants that create different strains in response to an applied stress, so the determination of average cluster strain from a single peak position is not very accurate and it is preferable to average over all peaks. The results are shown in Table 2.

In a Williamson–Hall analysis (Williamson & Hall, 1953), where there is non-uniform r.m.s. strain (ε) and small crystallites of diameter t, the peak width is broadened according to

$$\frac{\beta\cos(\theta)}{\lambda} = \varepsilon S + \frac{0.9}{t}, \qquad (2)$$

where θ is the Bragg diffraction angle at the centre of a peak, λ is the wavelength and $\beta = 2\Delta\theta$ is the peak full-width at half maximum (FWHM; Jeffrey, 1971). A linear fit to a plot of peak width against peak position S, gives the average particle diameter from the intercept and the average magnitude of the non-uniform r.m.s. strain from the slope. When the non-uniform strain is zero this reduces to the well known Scherrer equation for determining particle size. The non-uniform strain is caused by defects such as plastic or elastic deformation, dislocations, site disorder and stacking faults.

Fig. 3 shows the bismuth peak-width measurements made by Lorentzian peak-fitting to the XRD scans from six bismuth samples. We cannot resolve closely spaced peaks when the individual peaks are relatively broad due to the small size of the clusters. Some of the apparent noise in the Williamson–Hall analysis is due to peak broadening because of overlapping peaks. Only the sample labelled 'Bi oxide' had β-Bi_2O_3 peaks in the GIXRD scans, and the other five samples had a thin layer of oxide on the surface that was insufficient to create oxide peaks. This difference in oxide thickness is presumably a result of the preparation conditions. Table 2 shows the non-uniform strain and diameter determined by linear least-squares fits to the experimental data in Fig. 3, and also shows the uniform strain determined by peak shift. The uncertainties in Table 2 are from the linear least-squares fits. The four largest oxide peak widths gave large uncertainties in oxide width and non-uniform strain and are not included in Fig. 3 or Table 2. The diameter and magnitude of strain in Table 2 measured from the oxidized sample is consistent with the calculated patterns fitted to the GIXRD in Fig. 2. The BIO1 and BIO2 in the second sample batch made have a similar size to the oxidized sample, but a higher non-uniform strain. The averaged results for the third batch of clusters (BIAO17, 19 and 24) indicates that they tend to have a smaller diameter (confirmed by FEG SEM micrographs) than the initial oxidized sample, and a higher non-uniform strain. Within experimental uncertainties the uniform strain is compressive owing to oxide formation in comparison to clusters without oxide detectable by XRD, which have a small tensile uniform strain. Small-diameter oxidized clusters would be required to test this. A more advanced Warren analysis of the peak shape and broadening using Fourier transform coefficients (Noyan & Cohen, 1987) would be required to characterize the defect density (Sanders *et al.*, 1995; Ungar *et al.*, 1998, 2001), but this has not been attempted here owing to the anisotropy and texture in the bismuth samples.

Fig. 4 shows a section from an HRTEM micrograph of a cube-shaped bismuth cluster. The electron-beam direction relative to the crystal (B) is B = [2,−2,1] in the cluster core

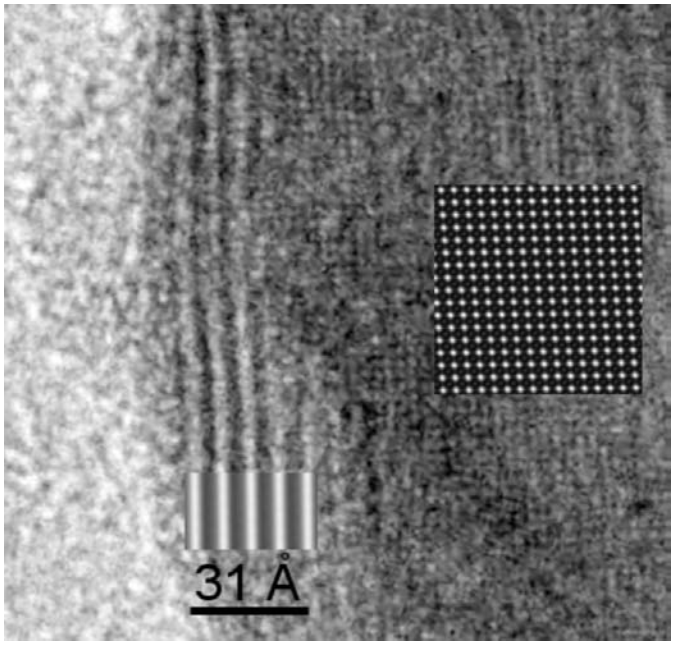

Figure 4
HRTEM micrograph of B = [2,−2,1] bismuth nanocluster and a multislice simulation for 375 Å thick bulk bismuth. A simulation for B = [2,−5,3] (*i.e.* tilted slightly off B = [1,−2,1]) of 405 Å thick β-Bi_2O_3 has been inserted near the edge of the cluster.

with crossed (1,0,−2) and (0,−1,−2) lattice fringes of 3.28 Å at 93°. The surface oxide has a dominant fringe of 7.8 Å which matches the *a* lattice parameter of β-Bi_2O_3. Multislice TEM image simulations with *JEMS* Version 3.05 were used to aid in the interpretation of experimental images (http://cimes-g1.epfl.ch/CIOL/ems.html; Stevens *et al.*, 2006). For the matching, the lattice-fringe spacings and the angles between crossed fringes are measured on the experimental micrographs. These are matched to the beam directions and excited diffraction vectors calculated for various candidate crystal structures. In the simulations, microscope image parameters are varied, such as defocus, specimen vibration and drift and specimen parameters: crystal thickness and orientation. The simulations often produce a greater contrast than the experimental micrograph, even though the geometry of the fringes matches well. Often the more diffuse and noisy background in images is due to CCD noise, inelastic scattering or thin oxide on a cluster core which is either ignored or not taken into account in the simulations. For computational speed the simulations also use defocus-spread-envelope functions to account for a finite filament source and energy spread, instead of summing over many partially coherent point sources. A Jeol 2010 LaB6 was used for HRTEM, which has a spherical aberration coefficient (Cs) of 1.0 mm. An envelope defocus spread of 100 Å and a near Scherzer defocus of 610 Å were used throughout. The loss of crossed fringes in the oxide indicates that the oxide is slightly tilted away from a high-symmetry zone axis so a lower symmetry B = [2,−5,3] has been used in the multislice simulations. The oxide is 20–30 Å thick in this micrograph, which is larger than the mean calculated from the Debye–Scherrer results, but this is within the experimental uncertainties. This is reasonable as not all clusters are oxidized to the same thickness as the facets of the cluster core present different faces to the atmosphere and it is unlikely or impossible for the oxide on the surface of the clusters to form a single coherent crystalline structure and still cover the entire cluster surface. The lower frequency (a periodicity of four bismuth lattice fringes) Moiré fringes in the top right of Fig. 4 indicate that the top and bottom surfaces on the cluster are also oxidized.

Figs. 5, 6 and 7 show HRTEM micrographs of oxidized bismuth clusters. Fig. 5 shows a crossed lattice-ring image of the oxide and an inset simulation for the B = [1,−2,1] of 182 Å thick β-Bi_2O_3. The fringes in the bismuth core are not as clear as in Fig. 4, even though they are both for B = [2,−2,1] in the cluster core, and this indicates that it is difficult to excite clear crossed lattice-fringe images in the oxide and core simultaneously owing to a small misorientation between the crystal structures. A dislocation in the bismuth core has been circled to show one of the defects that contributes to the peak broadening in the GIXRD scans. Fig. 6 shows a smaller 200 Å diameter cluster and even though the core has the same orientation as cores of the larger 40 nm diameter clusters in Figs. 4 and 5, the covering oxide has a different orientation of B = [0,1,−1] rather than the earlier B = [1,−2,1] for β-Bi_2O_3. Fig. 7 shows a micrograph of several coalesced clusters, which is notable because it has simultaneously excited crossed-latticed fringes in the oxide on two intersecting faces of a facetted cluster. It is possible for β-Bi_2O_3 to form coherent

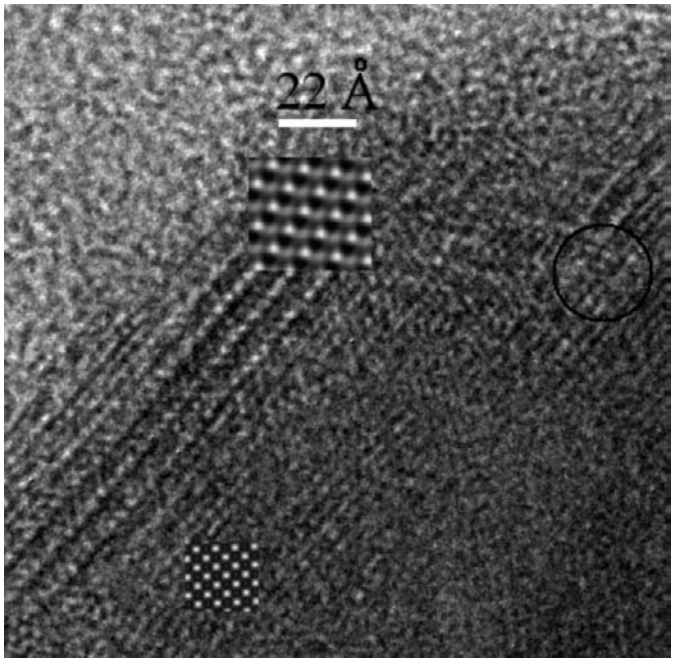

Figure 5
Fringes in B = [2,−2,1] and inset simulation for a 375 Å thick Bi core, and B = [1,−2,1] β-Bi_2O_3. A simulation for B = [1,−2,1] of 182 Å thick β-Bi_2O_3 has been inserted near the edge of the main cluster. The circled area indicates a dislocation in the bismuth core.

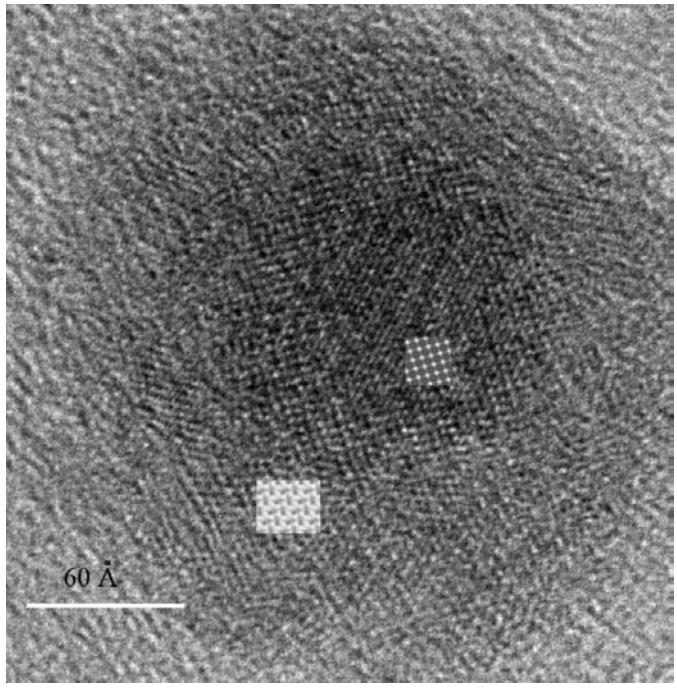

Figure 6
B = [2,−2,1] of 120 Å diameter Bi core, with (1,0,−2) and (0,−1,−2) fringes of 3.28 Å, (−1,1,4) fringes of 2.37 Å and matching simulation 118 Å thick, and oxide in B = [0,1,−1] β-Bi_2O_3 with (111) fringes of 3.91 Å and (200) fringes of 3.87 Å with matching simulations 57 Å thick.

crystalline domains on adjoining faces of facetted clusters to achieve a minimum energy configuration.

5. Discussion

TEM has shown that the orientation of the oxide shell changes to maintain the correct epitaxic relationship on each face of the bismuth core. The 320 ± 40 Å average bismuth core particle diameter and an average β-Bi_2O_3 oxide thickness of 20 ± 5 Å, has been calculated from the width of the peaks in the GIXRD pattern and by comparison with Debye–Scherrer simulations. The HRTEM observations showed an oxide thickness of 20–50 Å. A Williamson–Hall analysis of the peak broadening showed that the oxidized sample had a non-uniform strain of $0.25 \pm 0.08\%$ in a bismuth core of 350 ± 80 Å, compared with $0.5 \pm 0.1\%$ non-uniform strain in the 260 ± 50 Å diameter for clusters without detectable oxides, and 0.4 ± 0.1 and $0.4 \pm 0.2\%$ non-uniform strain in the 400 Å diameter clusters without detectable oxides. Calculations from the peak shifts showed that the oxidized clusters were in $-0.11 \pm 0.06\%$ uniform compressive strain, but the clusters without detectable oxides only have a small tensile strain. The clusters produced by the HV system are more oxidized and have less non-uniform strain than those deposited in the UHV system.

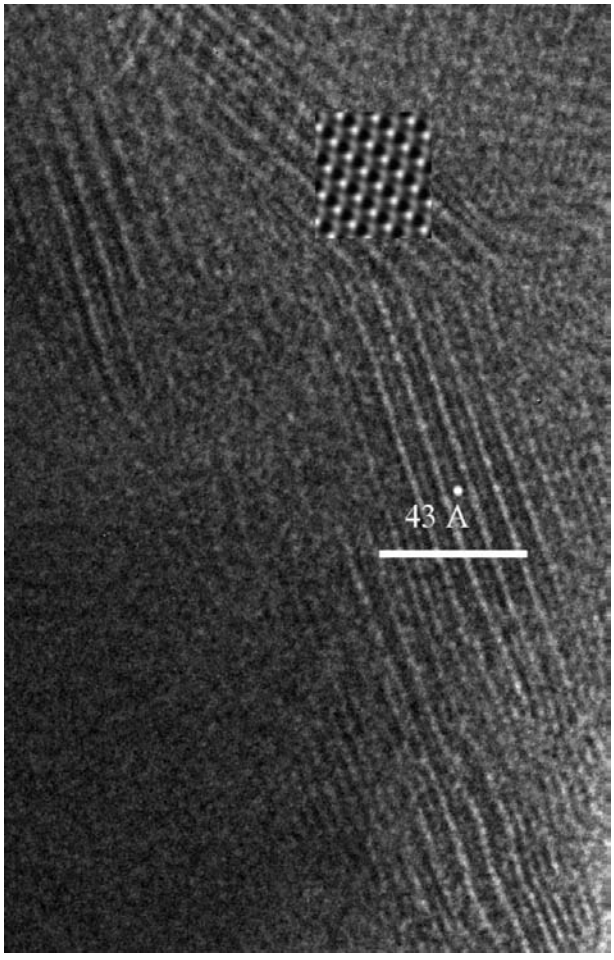

Figure 7
Faint fringes in bismuth, and clear crossed fringes in $B = [1,-2,1]$ β-Bi_2O_3 on a facetted cluster. Another cluster is visible in the top right corner of the image. A simulation for $B = [1,-2,1]$ of 182 Å thick β-Bi_2O_3 has been inserted near the edge of the main facetted cluster.

It is unusual for β-Bi_2O_3 to be the dominant bismuth oxide phase at room temperature. Although the structure of bismuth in 150–400 Å diameter powder prepared by an aerosol flow condenser in an oxygen-free environment, and then oxidized in ambient air, has been previously observed using a conventional laboratory X-ray tube, the oxide phase was not identified or compared with phase diagrams or HRTEM observations (Wegner *et al.*, 2002).

The clusters will probably progressively oxidize with time and the oxidation may not have been completed when the X-ray diffraction experiments were completed. Repeat measurements would be required to confirm this. The HRTEM observations were completed after the initial GIXRD measurements at SSRL, which is consistent with ongoing oxidation skewing the TEM oxide thickness to higher values than indicated by GIXRD. Earlier research (Wegner *et al.*, 2002) suggests that the introduction of trace amounts of oxygen during particle production forms a passivating oxide layer at the bismuth surface that is either too thin to be detected by XRD or is amorphous. Particles synthesized in an oxygen-free condenser atmosphere rapidly become more heavily oxidized in ambient air.

6. Conclusions

Synchrotron radiation experiments have shown that the dominant oxide type on bismuth clusters is β-Bi_2O_3. It is unusual for β-Bi_2O_3 to be the dominant bismuth oxide phase at room temperature. The width of the GIXRD peaks indicated that the bulk bismuth core of the clusters has an average diameter of 320 ± 40 Å and an average oxide thickness of 20 ± 5 Å. HRTEM indicates a typical oxide thickness of 20–50 Å and whilst the oxide is in some cases broken into smaller domains on each facet of the clusters surface, in other cases it can form a crystal structure on adjoining faces with a well defined grain boundary. HRTEM and XRD show that the bismuth core has the hexagonal structure of bulk bismuth.

This project was funded by NZ FRST NERF contract CO8X0409-Multiscale Modelling. Thanks to Dr R. Tilley and D. Flynn of VUW SCPS and the MacDiarmid Institute who provided access to a Jeol 2010 HRTEM. Drs S. Hendy, N. Laycock, M. Ryan and B. Hall of IRL are also acknowledged for assistance with this research. Portions of this research were carried out at the Stanford Synchrotron Radiation Laboratory, a national user facility operated by Stanford University on behalf of the US Department of Energy, Office of Basic Energy Sciences. Dr M. P. Ryan of Imperial College London is thanked for hosting B. Ingham.

References

Benbow, R. L. & Hurych, Z. (1976). *Phys. Rev. B*, **14**, 4295–4303.

Birkholz, M. (2006). *Thin Film Analysis by X-ray Scattering*, equation 2.17, pp. 70–74. New York: John Wiley.
Blower, S. K. & Greaves, C. (1988). *Acta Cryst.* C**44**, 587–589.
Cai, J. P. & Lyon, S. B. (2003). Paper CO64: Corrosion Science in the 21st Century, 6–11 July 2003. UMIST, Manchester.
Cucka, P. & Barrett, C. S. (1962). *Acta Cryst.* **15**, 865–872.
Flüeli, M. (1989). Ph.D. Thesis, p. 796. Ecole Polytechnique Federale de Lausanne, EPFL, France.
Hall, B. D., Flueli, M., Reinhard, D., Borel, J. P. & Monot, R. (1991). *Rev. Sci. Instrum.* **62**, 1481–1488.
Hall, B. D., Ugarte, D., Reinhard, D. & Monot, R. (1995). *J. Chem. Phys.* **103**, 2384–2394.
Harwig, H. A. (1978). *Z. Anorg. Allg. Chem.* **444**, 151–166.
Harwig, H. A. & Gerards, A. G. (1978). *J. Solid State Chem.* **26**, 265–274.
Harwig, H. A. & Gerards, A. G. (1979). *Thermochim. Acta*, **28**, 121–131.
Jeffrey, J. W. (1971). *Methods in X-ray Crystallography*, pp. 83–86. New York: Academic Press.
Lin, Y.-M., Dresselhaus, M. S. & Ying, J. Y. (2000). *Adv. Chem. Eng.* **27**, 167–203.
Noyan, I. C. & Cohen, J. B. (1987). *Residual Stress Measurement by Diffraction and Interpretation*, ch. 8. New York: Springer-Verlag.
Parquez, G., Natali, F., Brown, S., Ingham, B., Hendy, S., Stevens, K. & Toney, M. (2007). Proc. of AMN3 Int. Conf. on Advanced Materials and Nanotechnology, 11–16 February 2007. Wellington, New Zealand.
Rez, D., Rez, P. & Grant, I. (1994). *Acta Cryst.* A**50**, 481.
Sammes, N. M., Tompsett, G. A., Nafe, H. & Aldinger, F. (1999). *J. Eur. Ceram. Soc.* **19**, 1801–1826.
Sanders, P. G., Witney, A. B., Weertman, J. R., Valiev, R. Z. & Siegel, R. W. (1995). *Mater. Sci. Eng. A*, **204**, 7–11.
Shuk, P., Wiemhofer, H. D., Guth, U., Gopel, W. & Greenblatt, M. (1996). *Solid State Ion.* **89**, 179–196.
Stevens, K. J., Cheong, K. S., Knowles, D. M., Laycock, N. J., Brown, S. A. & Hendy, S. C. (2005). *Curr. Appl. Phys.* **6**, 453–456.
Stevens, K. J., Ingham, B., Toney, M. F., Brown, S. A., Lassesson, A., van Lith, J., Hendy, S. & Ryan, M. P. (2006). Oral presentation and paper at 4th Int. Workshop on Materials Issues Governing the Performance of Advanced 21st Century Energy Systems, 27 February to 1 March 2006. Te Papa, Wellington, New Zealand.
Stevens, K. J., Ingham, B., Toney, M. F., Brown, S. A., Partridge, J. & van Lith, J. (2005). Poster and paper at 14th AINSE Conference on Nuclear and Complementary Techniques, 20–22 November 2005. Wellington, New Zealand.
Ungar, T., Gubicza, J., Hanak, P. & Alexandrov, I. (2001). *Mater. Sci. Eng. A*, **319–321**, 274–278.
Ungar, T., Ott, S., Sanders, P. G., Borbely, A. & Weertman, J. R. (1998). *Acta Mater.* **46**, 3693–3699.
Wegner, K., Walker, B., Tsantilis, S. & Pratsinis, S. E. (2002). *Chem. Eng. Sci.* **57**, 1753–1762.
Williamson, G. K. & Hall, W. H. (1953). *Acta Metall.* **1**, 22.
Witkowska, A., Rybicki, J. & Di Cicco, A. (2005). *J. Alloys Compd.* **401**, 135–144.
Wurl, A. (2003). Ph.D. thesis. University of Canterbury, New Zealand.